Iron Reduction in Profundal Sediments of Ultraoligotrophic Lake Tahoe under Oxygen-Limited Conditions

Meret Aeppli,* Geoffrey Schladow, Juan S. Lezama Pacheco, and Scott Fendorf

Cite This: *Environ. Sci. Technol.* 2023, 57, 1529−1537

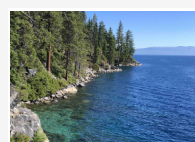Read Online

ACCESS | Metrics & More | Article Recommendations | Supporting Information

ABSTRACT: Increased periods of bottom water anoxia in deep temperate lakes due to decreasing frequency and depth of water column mixing in a warming climate may result in the reductive dissolution of iron minerals and increased flux of nutrients from the sediment into the water column. Here, we assessed the sediment properties and reactivities under depleted oxygen concentrations of Lake Tahoe, a deep ultraoligotrophic lake in the Sierra Nevada mountain range. Using whole-core incubation experiments, we found that a decrease in dissolved oxygen concentration in the top 2 cm of the sediment resulted in an extension of the microbial iron reduction zone from below 4.5 to below 1.5 cm depth. Concentrations of reactive iron generally decreased with sediment depth, and microbial iron reduction seemingly ceased as concentrations of Fe(II) approximated concentrations of reactive iron. These findings suggest that microorganisms preferentially utilized reactive iron and/or iron minerals became less reactive due to mineral transformation and surface passivation. The estimated release of iron mineral-associated phosphorus is not expected to change Lake Tahoe's trophic state but will likely contribute to increased phytoplankton productivity if mixed into surface waters.

Sediment characterization and whole-core incubation

Sediment sampling

In-situ conditions — Anoxic conditions — Fe(II)

KEYWORDS: *lake sediment, iron reduction, nutrient release, anoxia, sediment mineralogy, whole-core incubations*

INTRODUCTION

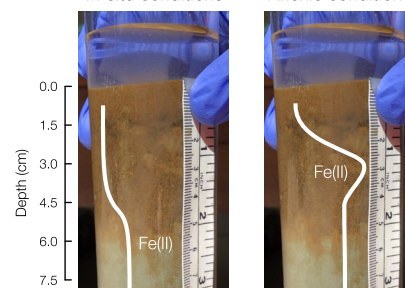Climate change causes surface waters in temperate lakes to warm,[1] leading to more stable thermal stratification of the water column and, thus, lower frequency and depth of water-column mixing.[2−5] As a consequence, isolated bottom waters are not consistently replenished with oxygen and can experience periods of hypoxia and possibly anoxia.[6−8] Hypolimnetic oxygen depletion causes a shift in organic matter degradation from aerobic to anaerobic pathways,[9,10] which can have serious ecological consequences if reduced compounds and nutrients are released from the sediment into the water column.[11,12] Deep, oligotrophic lakes in mountain regions are particularly susceptible to such effects of climate change, as these lakes are sensitive to nutrient loading[13] and because climatic warming typically occurs at a faster rate in mountain regions than regions at lower elevation.[14]

Lake Tahoe is a deep, ultraoligotrophic lake in the central Sierra Nevada on the California-Nevada (United States) border that serves as an indicator for effects of climate change on oligotrophic lakes worldwide. The annual average surface water temperature of Lake Tahoe has increased mainly as a result of rising air temperatures at an overall rate of 0.21 °C per decade.[15] Simulations of lake thermal structure showed that Lake Tahoe will likely cease to mix to the bottom after ∼2060 in a scenario in which greenhouse gas emissions increase

rapidly throughout the 21st century.[2,5] Should the lake fail to completely mix for more than 6 years in a row, hypolimnetic dissolved oxygen concentrations are expected to approach zero.[5] Under such conditions, ferric iron can be used as an electron acceptor in anaerobic microbial respiration.[16−18] Given that sediments of Lake Tahoe are rich in iron,[12] this respiration pathway is expected to become a key determinant of biogeochemical conditions in the hypolimnion as dissolved oxygen concentrations decrease. Ferric iron typically occurs as a particulate phase, e.g., in iron oxyhydroxides or ferric iron-containing clay minerals. Reduction of these particulate phases results in the formation of ferrous iron, which can desorb from the particulate surface and be released into the water column where it can stimulate phytoplankton productivity[19−21] or precipitate as iron oxyhydroxide under oxic conditions, forming particles and thereby decreasing water clarity.[12,22] Reductive dissolution of ferric iron minerals can also release adsorbed or coprecipitated phosphorus into sediment pore-

water and the water column, further alleviating nutrient limitations on phytoplankton productivity.[23−25] Substantial knowledge gaps exist regarding the mineralogy and redox state of iron in the sediments of Lake Tahoe, yet these factors determine if and how fast iron can be microbially reduced.[26−29] Assessing the susceptibility of iron reduction rates to decreasing dissolved oxygen concentrations is key to anticipate the consequences of increasing lake temperatures on the release of reduced compounds and nutrients from the sediment.

Here, we study the elemental composition and redox state of the profundal sediment of Lake Tahoe as a function of sediment depth and combine these measurements with characterizations of sediment mineralogy by means of X-ray diffractometry and X-ray absorption spectroscopy. To assess changes in iron reduction with sediment depth and shifts in iron reduction as a function of dissolved oxygen concentration, we performed whole-core incubation experiments at three oxygen levels (0.1%, 5.5%, and 21% atmospheric oxygen). We assessed changes in the redox state and reactivity of iron during the incubations.

■ MATERIALS AND METHODS

Sediment Sampling. Sediment samples were collected from aboard the University of California (UC) Davis research vessel R/V John LeConte on September 28, 2020. A box corer (area 0.3 m², depth 1.5 m) deployed from the boat was used for sample collection at 449 m depth (42°59′19.1″ N, 108°23′58.6′′ W). Samples were collected from a single location, as profundal sediment characteristics are fairly homogeneous.[12] On deck, minimally disturbed individual samples were subsampled from a single box-core grab into clear acrylic tubes (inner diameter 4.4 cm, 0.32 cm wall thickness) cut at ∼20 or ∼60 cm length (Tap Plastics). Samples consisted of the top ∼15 or ∼35 cm of sediment and ∼5 or ∼20 cm of water, respectively. The tubes were sealed by using butyl rubber stoppers and Parafilm. Duplicate cores for in situ sediment characterization were frozen ∼2 h after collection, cut into 1.5 cm wide slices, sealed into Mylar bags with oxygen scrubbers, and stored at −20 °C until analysis. Cores for the incubation experiments were stored upright at 4−10 °C until they were used in the experiments.

Whole-Core Incubation Experiments. Cores were incubated in airtight half-gallon glass jars at 5 °C at three atmospheric oxygen levels of 0.1%, 5.5%, and 21% for 74 days (see Figure S6 for photos of the cores). Prior to incubation, cores were preincubated for 11 weeks at 10 °C to ensure that monitored processes were not an artifact of sampling. For each treatment, duplicate cores were prepared by adapting the water level above the sediment-water interface to 2 cm height. Glass jars were flushed with pure nitrogen (0.1% atmospheric oxygen), a mix of nitrogen and compressed air (5.5% atmospheric oxygen, gases were mixed using a Cole-Parmer Masterflex Variable-Area Flowtube), or compressed air (21% atmospheric oxygen). The oxygen concentration in the jars was checked after flushing and before each sampling time point using optical oxygen sensor spots and an oxygen meter (PreSens). Measured values remained within 0.1−0.2% for the 0.1% atmospheric oxygen treatment, 5.5−5.7% for the 5.5% atmospheric oxygen treatment, and at 21% for the 21% atmospheric oxygen treatment throughout the experiment. At selected time points during the experiment (i.e., at 3, 8, 15, 37, 57, and 74 d), dissolved oxygen profiles were measured in the

cores using an oxygen microsensor mounted on a motor stand (UniSense). Profiles were recorded within 5 min of opening the glass jars from 1 cm above the sediment-water interface to 3.5 cm sediment depth at 1 mm intervals. pH was measured directly in the water overlaying the sediments in each core (Figure S10). In addition, sediment and water aliquots (0.25 mL aliquots from 0.5 cm above the sediment−water interface and from 0.5 1.5, 3, 4.5, 6.0, and 7.5 cm sediment depth) were collected from the cores using a cutoff syringe and in a clockwise fashion as the experiment progressed (illustration in Figure S5). Samples from duplicate cores were pooled without any further treatment and suspended into deoxygenated, deionized water (0.5 mL of sample into 4.5 mL of deoxygenated, deionized water). The diluted samples were used in aqueous and solid-phase analyses as described below. Sediment and water sampling was performed under constant nitrogen flow to avoid oxidation of ferrous iron and sulfide in the sample aliquots. Glass jars containing cores were resealed after sampling and flushed as described above.

Aqueous-Phase Analysis. Diluted sediment and water samples collected during the incubation experiments were filtered (0.22 μm poly(ether sulfone) (PES)) for aqueous-phase analysis. Dissolved sulfide levels were determined on freshly collected and filtered samples using the *N,N*-dimethyl-*p*-phenylenediamine method.[30] No sulfide was detected in any of the samples. Dissolved ferrous iron concentrations were determined after extraction of unfiltered samples in 0.5 M HCl for 1 h followed by filtration (0.22 μm PES) using the ferrozine method.[31] Colorimetric measurements for sulfide and ferrous iron were performed on a microplate reader (Synergy 2, BioTek).

Solid-Phase Analysis and Chemical Extractions. Cores that were frozen after collection (referred to as in situ cores, see above) were used for solid-phase analysis. Frozen core slices of 1.5 cm width were thawed and dried in an anoxic glovebag and subsequently finely ground with a mortar and pestle. Total elemental composition of the samples was determined using X-ray fluorescence spectroscopy (Spectro Xepos HE XRF Spectrometer) and, in the case of C and N, elemental analysis (NA1500, Carlo Erba Elemental Analyzer).

Chemical extractions were performed on sediments collected from in situ cores and from the incubated cores at the end point of the experiment in 1.5 cm intervals. Samples were extracted in deionized water (2 mL of sample per 10 mL) and hydrochloric acid 0.5 M (2 mL of sample per 5 mL) in 15 mL Falcon tubes. The sample suspensions were shaken for 2 h and centrifuged (3000 rpm; 15 min). The supernatant was then decanted and filtered (0.22 μm PES). Aqueous concentrations of Mn were determined on water extracts using an inductively coupled plasma (ICP) optical emission spectrometer (ICAP 6300 Duo View, Thermo). Concentrations of ferrous and total iron were determined on the acid extracts using the ferrozine method (see above) and hydroxyl-amine as reducing agent.[32]

Mediated Electrochemical Measurements. Diluted sediment samples collected during the incubation experiments under a nitrogen flow were immediately frozen at −20 °C for mediated electrochemical measurements to avoid changes in the redox state of iron during sample collection. Mediated electrochemical reduction (MER) and oxidation (MEO) were used to determine the electron accepting capacity (EAC) and donating capacity (EDC) of the samples. The electrochemical setup consisted of an eight-channel potentiostat (model
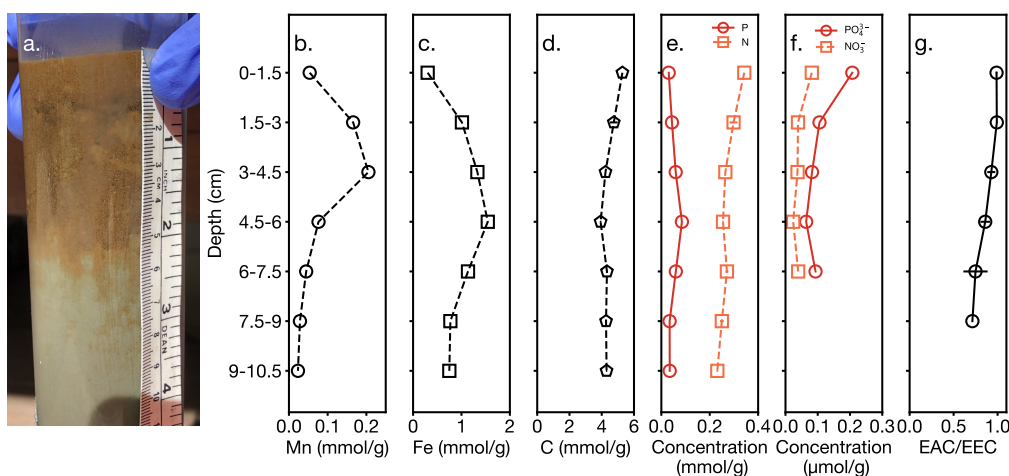
Figure 1. Sediment profile. (a) Photo of a sediment core and corresponding concentrations of (b) total manganese, (c) total iron, (d) total carbon, (e) total phosphorus and nitrogen, and (f) dissolved phosphate and nitrate. (g) Redox state of sediment expressed as ratio of EAC to total EEC, which is equal to the sum of EAC and EDC. Error bars in panels d–f represent duplicate measurements on single samples. Figure S2 shows the data in panels b–e as weight percentages and molar ratios of C/N and Fe/P with depth. Analyses were performed on sediment cores that were frozen after collection to represent in situ conditions in the lake.

1000C, CHInstrument, US) and eight electrochemical cells. Each cell consisted of a glassy carbon working electrode cylinder, which served as a reaction vessel (9 mL, GAZ 1 HTW), a platinum wire as counter electrode and separated from the working electrode compartment by a glass frit (PORE E tubes, ACE glass), and a Ag/AgCl reference electrode (Re1B, ALS). Reduction potentials are reported versus those of the standard hydrogen electrode herein.

Electrochemical measurements were performed in pH-buffered solutions at pH 5.0 (0.01 M acetate and 0.01 M KCl, 5 mL per electrochemical cell) and at applied reduction potentials for $E_{\mathrm{H}}^{\mathrm{MER}} = -0.57$ V in MER cells and $E_{\mathrm{H}}^{\mathrm{MEO}} = +0.82$ V in MEO cells. Under these conditions, we expect all ferric iron in oxyhydroxides[33] and clay minerals[34] as well as oxidized quinone groups in organic matter[35] to be reduced in MER, and we expect all ferrous iron,[26] sulfide,[36] and reduced quinone groups in organic matter[35] to be oxidized in MEO. Measurements were performed using the electron electron transfer mediators paraquat (1,1′-dimethyl-4, 4′-bipyridinium, standard reduction potential $E_{\mathrm{H}}^{0} = -0.46$ V[37]) in MER and ABTS (2,2′-azino-bis(3-ethylbenzothiazoline-6-sulfonic acid), $E_{\mathrm{H}}^{0} = +0.70$ V[38]) in MEO. These mediators were added to the electrochemical cells and equilibrated to the applied potentials prior to sample additions (final concentrations of reduced paraquat in the MER and oxidized ABTS in the MEO cells: 0.28 mM). For electrochemical measurements, the diluted sediment samples collected during the incubation experiments were further diluted by adding 100 μL of sample suspension to 300 μL of deionized water. Of these latter suspensions, we added 20 μL to each MER and MEO cell. Measurements were stopped at most 1 h after sample addition when currents had returned to baseline values that were measured before sample additions.

The EAC and EDC of the samples (in moles of electrons transferred per gram of dry sample) were determined by integration of reductive and oxidative current peaks, respectively, that resulted from sample additions to the electrochemical cells according to eqs 1 and 2.

$$\mathrm{EAC} = \frac{1}{F \cdot \mathrm{DW}} \cdot \int_{t_0}^{t_{\mathrm{end}}} I_{\mathrm{red}} \quad \mathrm{d}t \tag{1}$$

$$\mathrm{EDC} = \frac{1}{F \cdot \mathrm{DW}} \cdot \int_{t_0}^{t_{\mathrm{end}}} -I_{\mathrm{ox}} \quad \mathrm{d}t \tag{2}$$

where I_{red} and I_{ox} are the baseline-corrected reductive and oxidative currents, respectively (A), F is the Faraday constant, DW is the dry weight of the sample in grams, and t_0 and t_{end} (s) are the initial and final integration boundaries for each current peak. The electron exchanging capacity (EEC, in moles of electrons transferred per gram of dry sample) is the sum of EAC and EDC.

X-ray Diffractometry. X-ray diffractograms were recorded (MiniFlex 600, Rigaku) from 3° to 90° 2Θ (step size 0.02° 2Θ) in Bragg–Brentano geometry using Cu Kα radiation (40 kV and 40 mA) and a silicon strip detector (D/teX Ultra) or a two-dimensional (2D) hybrid pixel array detector (HyPix-400 MF). The identities of sediment components were determined using the SmartLab Studio-II software, published structure files for quartz (ICSD code 01-086-1629), and members of the feldspar group (sodium aluminum silicate (00-010-0033), sodium calcium aluminum silicate (01-079-1149), and potassium aluminum silicate (00-019-0931)).

X-ray Absorption Spectroscopy. Extended X-ray absorption fine structure (EXAFS) Fe K-edge spectra were collected at beamline 7–3 at the Stanford Synchrotron Radiation Lightsource (SSRL). Samples were prepared inside an anoxic chamber by pressing finely ground sample material into Al holders and covering them with Kapton tape. The Al holders were stored in an airtight jar under anoxic atmosphere before being rapidly transferred into the liquid He cryostat for analysis. The Si(220) double crystal monochromator was calibrated by setting the first inflection point of the absorption K-edge of a Fe metal foil to 7500 eV. For each sample, 3 scans were recorded in transmission mode using a Lytle detector. Spectra were processed and analyzed using the Demeter software package.[39] A linear combination-least-squares fitting was performed using reference spectra for ferrihydrite,[40] ferrosmectite, nontronite,[41] biotite,[42] and hornblende (Figure S3 and Table S2).
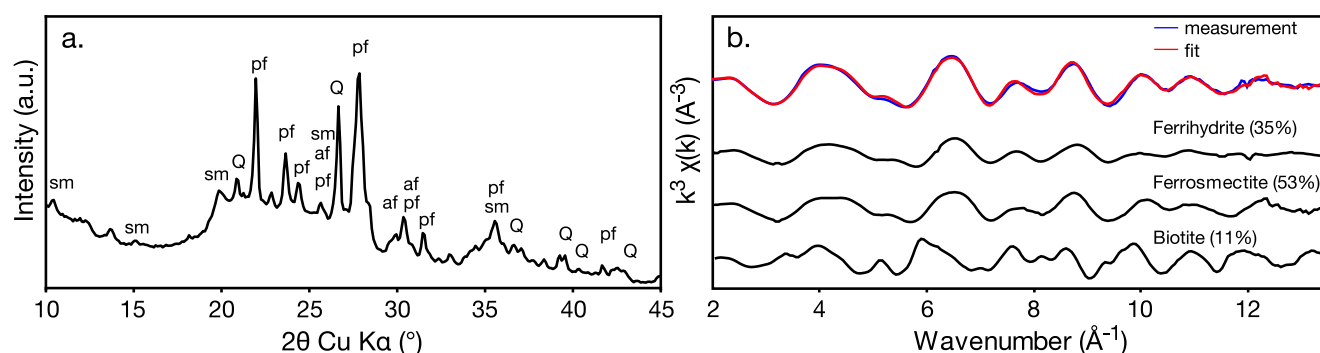
Figure 2. Mineralogy of exemplary sediment sample collected at 1.5−3 cm depth. (a) Representative X-ray diffractogram with characteristic peaks for quartz (Q) and members of the plagioclase feldspar (pf), alkali feldspar (af), and smectite (sm) groups. (b) Fourier transforms of the bulk Fe K-edge EXAFS spectrum (blue line) and linear combination-least-squares fit (red line; fitted values are shown on the right). References used in the fit are shown in black (ferrihydrite, a Fe oxyhydroxide; ferrosmectite and biotite, two Fe-containing phyollosilicate minerals). Results for samples collected at other depths are shown in Figures S3 and S4 and Table S2.

■ RESULTS AND DISCUSSION

Sediment Profile. Figure 1a shows a photo of the top 10 cm of a sediment core. The top ∼1 cm of sediment consisted of suspended material that moved with the overlaying water, whereas material below was more consolidated; consistent with these observations, sediment density increased from around 0.173 ± 0.08 g cm^{-3} at 0.5 cm to 0.262 ± 0.07 g cm^{-3} at 7.5 cm (Table S1). We determined the elemental composition of the sediment on the sediment cores that were frozen after collection. Manganese (Mn) and iron (Fe) concentrations peaked at 0.21 mmol g^{-1} at 3−4.5 cm and 1.54 mmol g^{-1} at 4.5−6 cm, respectively (Figure 1b,c; corresponding weight percentages in Figure S1a,b). To assess variations in the redox states of Mn and Fe as well as other solid-phase electron acceptors with depth, we quantified total electron accepting capacity (EAC) and electron donating capacity (EDC) of sediment samples using mediated electrochemistry. EAC reflected the response of particulate phases containing oxidized Mn or Fe[33,34,36] and quinone groups in dissolved and particulate organic matter[35] to strongly reducing conditions in electrochemical cells; EDC reflected the response of dissolved and solid-associated reduced Mn and Fe species and hydroquinone groups in dissolved and particulate organic matter[35] to strongly oxidizing conditions in electrochemical cells. The dissolved electron acceptors oxygen, nitrate, and sulfate are not electroactive in electrochemical cells and therefore do not contribute to EAC or EDC.[36] We note that dissolved sulfide, which produces an electrochemical response under oxidizing conditions,[36] was not detected in any of the sediment samples. Figure 1g shows that EAC/EEC decreased from fully oxidized (EAC/EEC = 0.99 ± 0.01) at 0−3 cm to partially reduced (EAC/EEC = 0.75 ± 0.14) at 6−7.5 cm. Consistent with this decrease, the concentrations of dissolved species contributing to EDC increased: the concentration of water-extractable Mn (which we assume to be Mn^{2+} under experimental conditions) increased with depth below 3 cm (Figure S7d), and the concentration of acid-extractable Fe(II) increased with depth below 4.5 cm (Figure 4a−c). Interpreted alongside the Mn and Fe concentration profiles in Figure 1b,c, these data indicate that microbial reductive dissolution of Mn oxyhydroxides was an important respiration pathway at 3−6 cm depth, while reductive dissolution of Fe oxyhydroxides was dominant below 4.5 cm depth. This interpretation was also consistent with the change in color from brown-black (the

color of Mn and Fe oxyhydroxides) to gray in the top 10 cm of the sediment (Figure 1a). In the top ∼1.5 cm, nitrate and oxygen were likely the dominant electron acceptors, as indicated by elevated nitrate concentrations of 0.08 μm g^{-1} compared to less than 0.04 μm g^{-1} below 1.5 cm (Figure 1f) and a rapid decrease in dissolved oxygen concentrations from 0 to 1.5 cm, as discussed below (Figure 3).

Total carbon (C) concentrations showed the inverse trend to Fe concentrations at 0−6 cm and stabilized at 4.3 ± 0.04 mmol g^{-1} below 6 cm (Figure 1d; corresponding weight percentages in Figure S1c). Concentration profiles of total nitrogen (N) mirrored those of total C (Figure 1e), and the C/N molar ratio of 15.7 ± 1.7 did not change systematically with depth (Figure S1e). Based on these C/N ratios, organic matter in the sediments primarily originated from land-derived organic matter, which has C/N ratios higher than 14−20, rather than C/N ratios of 4−10 associated with phytoplankton and aquatic macrophytes.[43] Total phosphorus (P) concentrations peaked at 0.08 mmol g^{-1} at 4.5−6 cm (Figure 1e), paralleling total Fe concentrations (Figure S2). Conversely, dissolved phosphate decreased with increasing depth in the top few centimeters (Figure 1f). These trends suggest that P entered the sediment from the water column as a dissolved phase and was partitioned into the solid phase a few centimeters into the sediment through the association with Fe phases. The molar ratio of Fe/P was 9.9 at 0−1.5 cm (and increased to values above 20 at 3−10.5 cm, Figure S1e), which was consistent with previous P/Fe ratios for Lake Tahoe sediments[12] and with P being primarily associated with Fe oxyhydroxides.[23−25]

X-ray diffraction and EXAFS analyses showed that Fe occurred primarily in the form of Fe oxyhydroxide and Fe-containing phyllosilicate clays. Figure 2 shows an exemplary X-ray diffractogram and EXAFS spectrum collected on the 1.5−3 cm sample as a representative example for Fe mineralogy in the top 7.5 cm of the sediment (see Figures S3 and S4 for other samples). Across 0−7.5 cm depth, the amorphous Fe oxyhydroxide mineral ferrihydrite accounted for 32−44% of Fe in the samples according to EXAFS analysis (Figure 2b and Table S2). The majority (56−68%) of Fe occurred in the form of Fe-containing phyllosilicate minerals based on EXAFS analysis. In addition to these Fe-containing minerals, X-ray diffractograms showed characteristic peaks for quartz and aluminumsilicates with various elemental compositions, including members of the plagioclase feldspar group
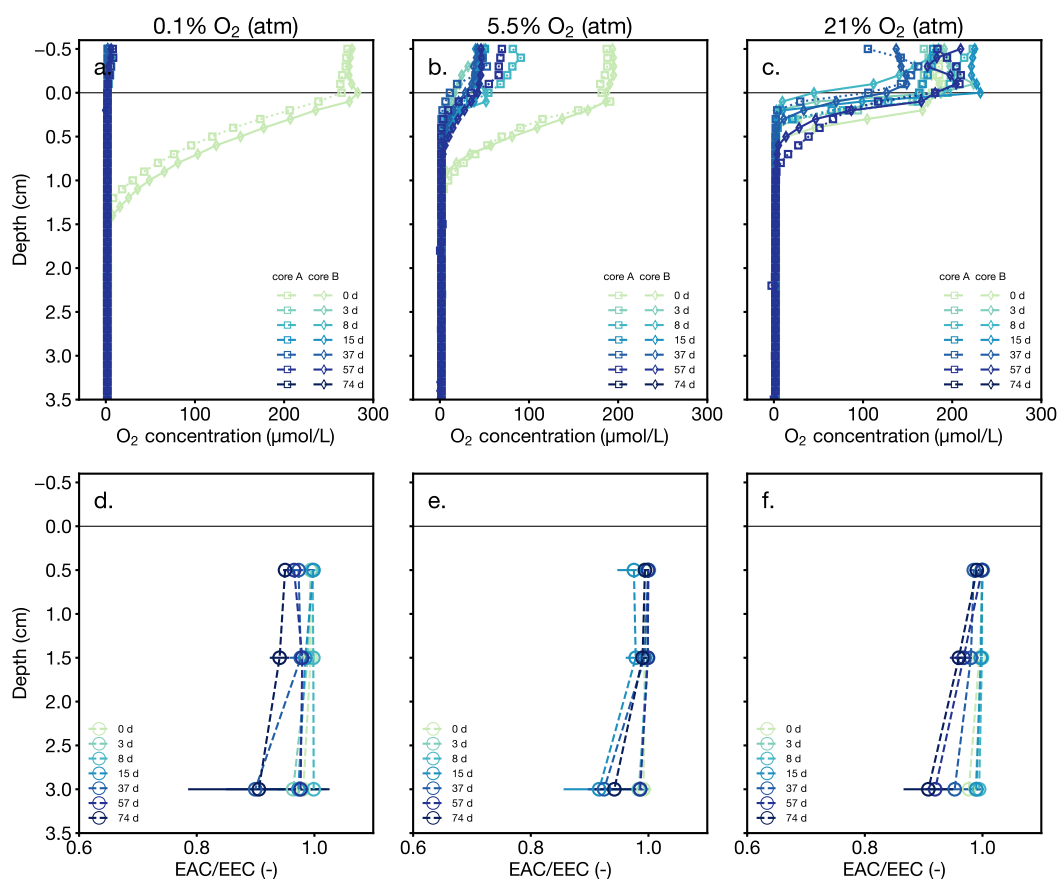
Figure 3. Dissolved oxygen and sediment redox profiles in whole-core incubation experiments under 0.1%, 5.5%, and 21% atmospheric oxygen. (a–c) Dissolved oxygen profiles collected at selected time points during the incubation experiments from 0.5 cm above the sediment–water interface at 0 cm down to 3.5 cm sediment depth at 1 mm intervals. Results are shown separately for the duplicate cores in each treatment. (d–f) Corresponding changes in the ratio of EAC to EEC (sum of EAC and EDC) of sediment samples collected at 0.5, 1.5, and 3 cm depth at selected time points during the incubation experiments. Error bars represent mean absolute deviations of duplicate measurements on each pooled sediment sample.

(containing Na and/or Ca) and alkali feldspar groups (containing K; see Figure S1a,b for Ca, Na, K, and Al concentration profiles).

Influence of Dissolved Oxygen Concentration on Sediment Profiles. To assess the effect of decreased dissolved oxygen concentration on sediment redox processes, we incubated whole sediment cores under three atmospheric oxygen levels (setup in Figure S5). We used treatments with 0.1 and 21% atmospheric oxygen as reference points for anoxic and oxic systems, respectively. In addition, we used an intermediate atmospheric oxygen concentration of 5.5% to mimic incomplete depletion of dissolved oxygen.

Figure 3a–c shows dissolved oxygen profiles recorded at selected time points throughout the incubation experiments. Initial profiles (light green) at the start of the experiments were similar for all of the treatments. Within the first 3 days, dissolved oxygen concentration at the sediment–water interface decreased to concentrations in the overlaying water in the 0.1% and 5.5% atmospheric oxygen treatments. Thereafter, concentration profiles remained constant over the course of the 74 day experiment. The 21% atmospheric oxygen treatment showed no systematic changes in profiles throughout the experiment. In the 5.5% and 21% atmospheric oxygen treatments, measured concentrations of dissolved oxygen in the water overlying the sediments were lower than calculated equilibrium concentrations of 82 μmol L^{-1} for 5% treatment

and 400 μmol L^{-1} for 21% treatment at 5 °C, presumably due to microbial oxygen consumption in the water column. Dissolved oxygen concentrations decreased rapidly with sediment depth in these treatments due to microbial consumption. No dissolved oxygen was detected below 1.5 cm in any of the treatments. The depth of oxygen penetration differed slightly between the cores, which was likely due to differences in the distribution of sediment layers along depth: in cores incubated under 0.1% and 5.5% atmospheric oxygen, the layer of unconsolidated material at the sediment–water interface extended further down than in cores incubated under 21% atmospheric oxygen (see photos in Figure S6), consistent with lower sediment density values for the former two (Table S1). We note that, under in situ conditions in the lake, we would expect dissolved oxygen to penetrate deeper into the sediment than in our experimental setup due to advective movement. This expectation is consistent with the in situ EAC/EEC and nitrate concentration profiles in Figure 1d,g, which indicate that aerobic and nitrate respiration were the dominant microbial respiration pathways at 0–3 cm depth.

We assessed how the redox state of the sediment changed as a consequence of changes in dissolved oxygen concentrations and associated shifts in microbial respiration pathways. Figure 3d–f shows EAC/EEC values of sediment samples collected from 0.5, 1.5, and 3 cm depths at selected time points during the incubation experiments. An EAC/EEC value of 1 indicates
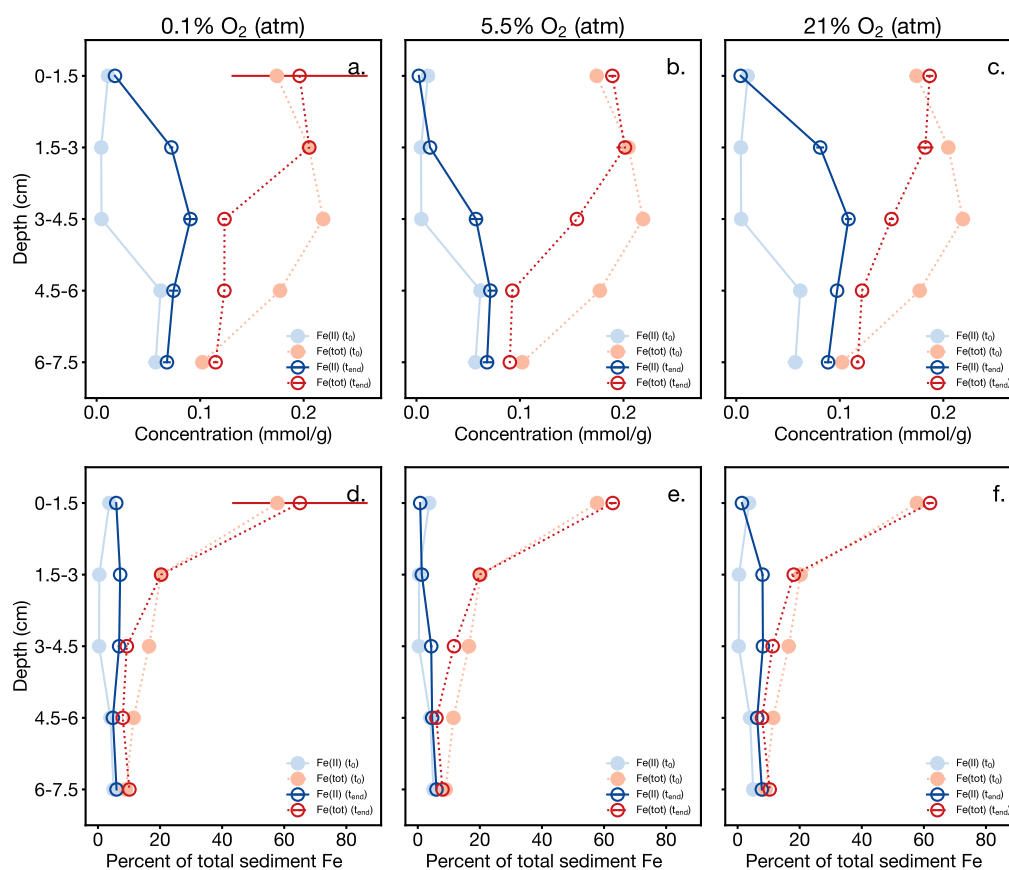
Figure 4. Fe(II) production dynamics in whole-core incubation experiments under 0.1%, 5.5%, and 21% atmospheric oxygen. (a−c) Profiles of acid-extractable Fe(II) and acid-extractable total Fe (Fe(tot), sum of acid-extractable Fe(II) and hydroxylamide-reducible Fe(III)) for the start (t_0, filled symbols, quantified on cores frozen upon collection) and the end (t_{end}, empty symbols, quantified on experimental cores at the end of incubation experiments) of the experiments. (d−f) Profiles of acid-extractable Fe(II) and acid-extractable Fe(tot) expressed as a percentage of total sediment Fe. Error bars represent mean absolute deviations of duplicate measurements on each pooled sediment sample.

a fully oxidized sample, whereas a value of 0 indicates a fully reduced sample. In all treatments, EAC/EEC decreased at a depth of 3 cm over the course of the experiments due to the buildup of EDC. The buildup corresponded to the formation of acid-extractable Fe(II) (Figure S9). This finding suggests that microbial Fe(III) reduction was the dominant pathway for microbial respiration, which was consistent with the absence of dissolved oxygen at this depth. The decrease in EAC/EEC at 0.5 cm was more pronounced in the 0.1% atmospheric oxygen treatment than in the other two treatments, presumably because oxygen was not available in the former treatment, and hence Fe(III) was the most thermodynamically favorable electron acceptor for microbial respiration. Accordingly, Fe(II) formation rates calculated from the EDC data at 0.5 cm depth were higher in the 0.1% atmospheric oxygen treatment with 0.6 μmol g^{-1} d^{-1} compared to 0.1 and 0.2 μmol g^{-1} d^{-1} in the 5.5% and 21% atmospheric oxygen treatments, respectively. In agreement with similar redox conditions across all cores below 1.5 cm depth, Fe(II) formation rates were similar for all treatments at 3 cm depth, with 1.3 μmol g^{-1} d^{-1} for the 0.1%, 1.0 μmol g^{-1} d^{-1} for the 5.5%, and 1.3 μmol g^{-1} d^{-1} for the 21% atmospheric oxygen treatments.

Iron Reduction Dynamics. We extended our analysis of changes in sediment redox state beyond 3 to 7.5 cm depth. Figure 4a−c compares profiles of acid-extractable Fe(II) at the onset of the experiment (quantified on sediments immediately frozen after collection, filled symbols) to profiles of acid-

extractable Fe(II) at the end point of the experiments after 74 days (quantified on treatment cores, empty symbols). Profiles were similar across all treatments below 1.5 cm, consistent with the absence of dissolved oxygen (Figure 3a−c). Elevated concentrations of acid-extractable Fe(II) were observed in the 0−1.5 cm depth interval for the 0.1% atmospheric oxygen treatment. The concentration of acid-extractable Fe(II) matched EDC within error in all treatments (Figure S9). Given that EDC represents the cumulative response of both dissolved and solid-phase associated reduced redox-active species, this suggests that Fe(II) was either dissolved or adsorbed to particulate surfaces or that it occurred as an easily extractable solid phase. The zone of microbial Fe reduction extended from 0−1.5 cm (0.1% atmospheric oxygen treatment) or 1.5 cm (remaining treatments) to 6−7.5 cm depth based on the increase in acid-extractable Fe(II) in this zone. Compared to the in situ conditions in Figure 1g, the upper end of the Fe reduction zone in our incubation experiments therefore extended upward from 4.5 cm to at least 1.5 cm (see Figure S11 for changes in EAC/EEC in the treatments). Therefore, the lack of oxygen in the top few centimeters of the sediment stimulated microbial Fe reduction in layers closer to the sediment−water interface.

Within the zone of microbial Fe reduction, we observed differences in the reactivity of the Fe phases. The concentration of acid-extractable total Fe, i.e., the sum of acid-extractable Fe(II) and hydroxylamine-reducible Fe(III),

was decreased at 3—6 cm depth in all treatments relative to the initial concentration profiles (Figure 4a—c). These trends indicate that Fe minerals became harder to reduce over the course of the incubations given that hydroxylamine-reducible Fe serves as a proxy for microbially reducible iron.[32] A possible explanation for this observation is the preferential use of easily reducible Fe minerals by iron-reducing microorganisms.[22,44,45] It is also possible that elevated Fe(II) concentrations at 3—6 cm depth caused the transformation of ferrihydrite into less reactive phases or resulted in passivation of mineral surfaces.[46] The in situ core showed the same trends of decreased acid-extractable total Fe concentrations below 4.5 cm (Figure 4a—c, filled symbols), suggesting that similar processes as those observed in our experiment were taking place under in situ conditions in these lower layers at 4.5—7.5 cm.

Panels d—f in Figure 4 show the same data as panels a—c but expressed as percentage of total sediment Fe. In the top 1.5 cm, around 65% of total Fe was reactive; this fraction decreased to around 10% in the lowest layer for both the initial material and the end-point material. The higher reactivity of Fe minerals closer to the sediment—water interface potentially results from the sedimentation of recently precipitated, highly amorphous iron oxide particles.[22,47] In the anoxic parts of both the experimental and in situ cores, microbial Fe reduction proceeded until 5—10% of Fe had been reduced. This finding suggests that the fraction of microbially reducible Fe was similar across the entire zone of Fe reduction. Given that Fe reduction in our experimental cores was not more extensive than in the in situ core at depths below 4.5 cm, we consider it likely that microbial Fe reduction would not proceed beyond 10% of the total sediment Fe even for longer incubation times. This is consistent with an observed cessation of Fe(II) production toward the end of our incubations (Figure S9).

Implications. Our work shows that microbial Fe reduction in Lake Tahoe's sediment currently occurs primarily at and below 4.5 cm depth. The upper limit of the Fe reduction zone significantly extended to 1.5 cm depth when the dissolved oxygen concentration at the sediment—water interface was reduced to zero in our experiments. Hypolimnetic dissolved oxygen concentrations are projected to decrease in response to decreased depth and frequency of lake mixing in the following decades,[2,5] and this decrease will likely cause the sediment Fe reduction zone to extend toward the sediment—water interface. Our results suggest that microbial Fe reduction will proceed until around 10% of total sediment Fe is reduced and that this value is determined by the amount of reactive Fe phases and Fe(II) accumulation. Fe(II) produced in the sediment may be released into the water column where it would be rapidly oxidized and precipitate as iron oxyhydroxides upon contact with oxygen.[12,22] While we consider it unlikely that Fe(II) is mixed into surface waters and induces algal blooms, the release of phosphorus during reductive dissolution of sediment iron minerals poses a bigger threat to lake ecology.[23—25] If we assume that 10% of Fe in the top 1.5 cm of sediment is reductively dissolved and phosphorus was homogeneously mixed into the entire lake water body, phosphorus concentrations in the water column would increase by around 1.2 μg L^{-1} (using a total lake volume[12] of 152 km^3) in line with previous findings by Beutel and Horne.[12] While this amount would not change the trophic status of Lake Tahoe, Beutel and Horne[12] suggested that it would result in a 40% increase in phytoplankton productivity. Therefore, there is a need for continuous monitoring of oxygen saturation in lake-bottom waters for early detection of internal nutrient loading in oligotrophic lakes.

ASSOCIATED CONTENT

Supporting Information

The Supporting Information is available free of charge at https://pubs.acs.org/doi/10.1021/acs.est.2c05714.

Sediment elemental composition and density, Fe K-edge EXAFS spectra and fitting results, X-ray diffractograms, schematic of experimental setup, photos of experimental cores, depth profiles for concentrations of Fe(II), total Fe, and water-extractable Mn, temporal changes in electron donating capacity and HCl-extractable Fe(II) during incubation experiments, depth profiles for electron accepting capacity (PDF)

AUTHOR INFORMATION

Corresponding Author

Meret Aeppli − Department of Earth System Science, Stanford University, Stanford, California 94305, United States; School of Architecture, Civil and Environmental Engineering, EPFL, Lausanne, Vaud 1015, Switzerland; orcid.org/0000-0003-3335-3673; Email: meret.aeppli@epfl.ch

Authors

Geoffrey Schladow − Department of Civil and Environmental Engineering, UC Davis, Davis, California 95616, United States; UC Davis Tahoe Environmental Research Center, Incline Village, Nevada 89451, United States

Juan S. Lezama Pacheco − Department of Earth System Science, Stanford University, Stanford, California 94305, United States; Stanford Synchrotron Radiation Lightsource, SLAC National Accelerator Laboratory, Menlo Park, California 94025, United States

Scott Fendorf − Department of Earth System Science, Stanford University, Stanford, California 94305, United States; orcid.org/0000-0002-9177-1809

Complete contact information is available at:
https://pubs.acs.org/10.1021/acs.est.2c05714

Notes

The authors declare no competing financial interest.

ACKNOWLEDGMENTS

REFERENCES

(1) Bates, B.; Kundzewicz, Z.; Wu, S.; Palutikof, J. *Technical Paper of the Intergovernmental Panel on Climate Change*; IPCC Secretariat: Geneva, Switzerland, 2008; p 210.

(2) Sahoo, G. B.; Forrest, A. L.; Schladow, S. G.; Reuter, J. E.; Coats, R.; Dettinger, M. Climate change impacts on lake thermal dynamics and ecosystem vulnerabilities. *Limnol. Oceanogr.* **2016**, *61*, 496−507.

(3) Butcher, J. B.; Nover, D.; Johnson, T. E.; Clark, C. M. Sensitivity of lake thermal and mixing dynamics to climate change. *Clim. Change* **2015**, *129*, 295−305.

(4) Schwefel, R.; Gaudard, A.; Wüest, A.; Bouffard, D. Effects of climate change on deepwater oxygen and winter mixing in a deep lake (Lake Geneva): Comparing observational findings and modeling. *Water Resour. Res.* **2016**, *52*, 8811−8826.

(5) Sahoo, G. B.; Schladow, S. G.; Reuter, J. E.; Coats, R.; Dettinger, M.; Riverson, J.; Wolfe, B.; Costa-Cabral, M. The response of Lake Tahoe to climate change. *Clim. Change* **2013**, *116*, 71−95.

(6) Zhang, Y.; Wu, Z.; Liu, M.; He, J.; Shi, K.; Zhou, Y.; Wang, M.; Liu, X. Dissolved oxygen stratification and response to thermal structure and long-term climate change in a large and deep subtropical reservoir (Lake Qiandaohu, China). *Water Res.* **2015**, *75*, 249−258.

(7) North, R. P.; North, R. L.; Livingstone, D. M.; Köster, O.; Kipfer, R. Long-term changes in hypoxia and soluble reactive phosphorus in the hypolimnion of a large temperate lake: consequences of a climate regime shift. *Glob. Change Biol.* **2014**, *20*, 811−823.

(8) Jankowski, T.; Livingstone, D. M.; Bührer, H.; Forster, R.; Niederhauser, P. Consequences of the 2003 European heat wave for lake temperature profiles, thermal stability, and hypolimnetic oxygen depletion: Implications for a warmer world. *Limnol. Oceanogr.* **2006**, *51*, 815−819.

(9) Matzinger, A.; Müller, B.; Niederhauser, P.; Schmid, M.; Wüest, A. Hypolimnetic oxygen consumption by sediment-based reduced substances in former eutrophic lakes. *Limnol. Oceanogr.* **2010**, *55*, 2073−2084.

(10) Maerki, M.; Müller, B.; Dinkel, C.; Wehrli, B. Mineralization pathways in lake sediments with different oxygen and organic carbon supply. *Limnol. Oceanogr.* **2009**, *54*, 428−438.

(11) Steinsberger, T.; Schwefel, R.; Wüest, A.; Müller, B. Hypolimnetic oxygen depletion rates in deep lakes: Effects of trophic state and organic matter accumulation. *Limnol. Oceanogr.* **2020**, *65*, 3128−3138.

(12) Beutel, M. W.; Horne, A. J. Nutrient Fluxes From Profundal Sediment of Ultra-Oligotrophic Lake Tahoe, California/Nevada: Implications for Water Quality and Management in a Changing Climate. *Water Resour. Res.* **2018**, *54*, 1549−1559.

(13) Burkholder, J. M.*Encyclopedia of Biodiversity;*Elsevier Inc., 2003; pp 649−670.

(14) Coats, R. Climate change in the Tahoe basin: regional trends, impacts and drivers. *Clim. Change* **2010**, *102*, 435−466.

(15) Tahoe: state of the lake report 2021. Available at https://tahoe. ucdavis.edu/sites/g/files/dgvnsk4286/files/inline-files/8_Physical_8. pdf Accessed 2022-12-29.

(16) Ehrlich, H. L.; Newman, D. K.; Kappler, A.*Ehrlich's Geomicrobiology;*CRC Press; Taylor & Francis Group: Boca Raton, FL, 2015.

(17) Nealson, K. H.; Saffarini, D. Iron and Manganese in Anaerobic Respiration: Environmental Significance, Physiology, and Regulation. *Annu. Rev. Microbiol.* **1994**, *48*, 311−343.

(18) Lovley, D. R. Dissimilatory Fe(III) and Mn(IV) reduction. *Microbiol. Rev.* **1991**, *55*, 259−287.

(19) Sorichetti, R. J.; Creed, I. F.; Trick, C. G. Evidence for iron-regulated cyanobacterial predominance in oligotrophic lakes. *Freshw. Biol.* **2014**, *59*, 679−691.

(20) Callieri, C.; Stockner, J. View of Picocyanobacteria success in oligotrophic lakes: fact or fiction? *J. Limnol.* **2000**, *59*, 72−76.

(21) Chang, C. C. Y.; Kuwabara, J. S.; Pasilis, S. P. Phosphate and Iron Limitation of Phytoplankton Biomass in Lake Tahoe. *Can. J. Fish. Aquat. Sci.* **1992**, *49*, 1206−1215.

(22) Davison, W. Iron and manganese in lakes. *Earth-Sci. Rev.* **1993**, *34*, 119−163.

(23) Schauser, I.; Chorus, I.; Lewandowski, J. Effects of nitrate on phosphorus release: comparison of two Berlin lakes. *Acta Hydrochim. Hydrobiol.* **2006**, *34*, 325−332.

(24) Welch, E. B.; Cooke, G. D. Internal Phosphorus Loading in Shallow Lakes: Importance and Control. *Lake Reserv. Manag* **2005**, *21*, 209−217.

(25) Jensen, H. S.; Kristensen, P.; Jeppesen, E.; Skythe, A. Iron:phosphorus ratio in surface sediment as an indicator of phosphate release from aerobic sediments in shallow lakes. *Hydrobiol* **1992**, *235−236*, 731−743.

(26) Aeppli, M.; Vranic, S.; Kaegi, R.; Kretzschmar, R.; Brown, A. R.; Voegelin, A.; Hofstetter, T. B.; Sander, M. Decreases in Iron Oxide Reducibility during Microbial Reductive Dissolution and Transformation of Ferrihydrite. *Environ. Sci. Technol.* **2019**, *53*, 8736−8746.

(27) Cutting, R. S.; Coker, V. S.; Fellowes, J. W.; Lloyd, J. R.; Vaughan, D. J. Mineralogical and morphological constraints on the reduction of Fe(III) minerals by Geobacter sulfurreducens. *Geochim. Cosmochim. Acta* **2009**, *73*, 4004−4022.

(28) Phillips, E. J.; Lovley, D. R.; Roden, E. E. Composition of Non-Microbially Reducible Fe(III) in Aquatic Sediments. *Appl. Environ. Microbiol.* **1993**, *59*, 2727−2729.

(29) Lovley, D. R.; Phillips, E. J. Availability of ferric iron for microbial reduction in bottom sediments of the freshwater tidal potomac river. *Appl. Environ. Microbiol.* **1986**, *52*, 751−757.

(30) Cline, J. D. Spectrophotometric determination of hydrogen sulfide in natural waters. *Limnol. Oceanogr.* **1969**, *14*, 454−458.

(31) Stookey, L. L. Ferrozine− a new spectrophotometric reagent for iron. *Anal. Chem.* **1970**, *42*, 779−781.

(32) Lovley, D. R.; Phillips, E. J. Rapid assay for microbially reducible ferric iron in aquatic sediments. *Appl. Environ. Microbiol.* **1987**, *53*, 1536−1540.

(33) Aeppli, M.; Voegelin, A.; Gorski, C. A.; Hofstetter, T. B.; Sander, M. Mediated Electrochemical Reduction of Iron (Oxyhydr-)Oxides under Defined Thermodynamic Boundary Conditions. *Environ. Sci. Technol.* **2018**, *52*, 560−570.

(34) Gorski, C. A.; Kluepfel, L. E.; Voegelin, A.; Sander, M.; Hofstetter, T. B. Redox Properties of Structural Fe in Clay Minerals: 3. Relationships between Smectite Redox and Structural Properties. *Environ. Sci. Technol.* **2013**, *47*, 13477−13485.

(35) Kluepfel, L. E.; Piepenbrock, A.; Kappler, A.; Sander, M. Humic substances as fully regenerable electron acceptors in recurrently anoxic environments. *Nat. Geosci.* **2014**, *7*, 195−200.

(36) Kluepfel, L. E.*Redox properties and dynamics of natural organic matter as assessed by mediated electrochemical analysis.* Ph.D. Thesis, ETH Zurich, 2015.

(37) Aeppli, M.; Babey, T.; Engel, M.; Lacroix, E. M.; Tolar, B. B.; Fendorf, S.; Bargar, J. R.; Boye, K. Export of Organic Carbon from Reduced Fine-Grained Zones Governs Biogeochemical Reactivity in a Simulated Aquifer. *Environ. Sci. Technol.* **2022**, *56*, 2738−2746.

(38) Gorski, C. A.; Kluepfel, L. E.; Voegelin, A.; Sander, M.; Hofstetter, T. B. Redox Properties of Structural Fe in Clay Minerals. 2. Electrochemical and Spectroscopic Characterization of Electron Transfer Irreversibility in Ferruginous Smectite, SWa-1. *Environ. Sci. Technol.* **2012**, *46*, 9369−9377.

(39) Ravel, B.; Newville, M. ATHENA, ARTEMIS, HEPHAESTUS: data analysis for X-ray absorption spectroscopy using IFEFFIT. *J. Synchrotron Radiat.* **2005**, *12*, 537−541.

(40) Maillot, F.; Morin, G.; Wang, Y.; Bonnin, D.; Ildefonse, P.; Chaneac, C.; Calas, G. New insight into the structure of nanocrystalline ferrihydrite: EXAFS evidence for tetrahedrally coordinated iron(III). *Geochim. Cosmochim. Acta* **2011**, *75*, 2708−2720.

(41) Noël, V.; Marchand, C.; Juillot, F.; Ona-Nguema, G.; Viollier, E.; Marakovic, G.; Olivi, L.; Delbes, L.; Gelebart, F.; Morin, G. EXAFS analysis of iron cycling in mangrove sediments downstream a lateritized ultramafic watershed (Vavouto Bay, New Caledonia). *Geochim. Cosmochim. Acta* **2014**, *136*, 211−228.

(42) Othmane, G.; Allard, T.; Morin, G.; Sélo, M.; Brest, J.; Llorens, I.; Chen, N.; Bargar, J. R.; Fayek, M.; Calas, G. Uranium Association with Iron-Bearing Phases in Mill Tailings from Gunnar, Canada. *Environ. Sci. Technol.* **2013**, *47*, 12695−12702.

(43) Meyers, P. A.; Teranes, J. L. In *Tracking Environmental Change Using Lake Sediments, Physical and Geochemical Methods;*Last, W., Smol, J., Eds.; Developments in Paleoenvironmental Research;Kluwer Academic Publishers: London, UK, 2001; Vol. 2; pp 239−269.

(44) Bray, M. S.; Wu, J.; Reed, B. C.; Kretz, C. B.; Belli, K. M.; Simister, R. L.; Henny, C.; Stewart, F. J.; DiChristina, T. J.; Brandes, J. A.; Fowle, D. A.; Crowe, S. A.; Glass, J. B. Shifting microbial

communities sustain multiyear iron reduction and methanogenesis in ferruginous sediment incubations. *Geobiology* **2017**, *15*, 678−689.

(45) Davison, W.; Dickson, D. Mössbauer spectroscopic and chemical studies of particulate iron material from a seasonally anoxic lake. *Chem. Geol.* **1984**, *42*, 177−187.

(46) Gadol, H. J.; Elsherbini, J.; Kocar, B. D. Methanogen Productivity and Microbial Community Composition Varies With Iron Oxide Mineralogy. *Frontiers in Microbiology* **2022**, *12*, 705501.

(47) Hilton, J.; Long, G.; Chapman, J.; Lishman, J. Iron mineralogy in sediments. A Mössbauer study. *Geochim. Cosmochim. Acta* **1986**, *50*, 2147−2151.